

Electron-capture supernovae in NS+He star systems and the double neutron star systems

Yun-Lang Guo,^{1,2,3}★ Bo Wang,^{3,4,5}† Wen-Cong Chen,⁶ Xiang-Dong Li,^{1,2}‡ Hong-Wei Ge,^{3,4,5}
Long Jiang⁶ and Zhan-Wen Han^{3,4,5}

¹*School of Astronomy and Space Science, Nanjing University, Nanjing 210023, China*

²*Key Laboratory of Modern Astronomy and Astrophysics, Nanjing University, Ministry of Education, Nanjing 210023, China*

³*University of Chinese Academy of Sciences, Beijing 100049, China*

⁴*Yunnan Observatories, Chinese Academy of Sciences, Kunming 650216, China*

⁵*International Centre of Supernovae, Yunnan Key Laboratory, Kunming 650216, China*

⁶*School of Science, Qingdao University of Technology, Qingdao 266525, China*

Accepted XXX. Received YYY; in original form ZZZ

ABSTRACT

Electron-capture supernovae (EC-SNe) provide an alternative channel for producing neutron stars (NSs). They play an important role in the formation of double NS (DNS) systems and the chemical evolution of galaxies, and contribute to the NS mass distribution in observations. It is generally believed that EC-SNe originate from e -captures on ^{24}Mg and ^{20}Ne in the massive degenerate oxygen-neon (ONe) cores with masses close to the Chandrasekhar limit (M_{Ch}). However, the origin of EC-SNe is still uncertain. In this paper, we systematically studied the EC-SNe in NS+He star systems by considering the explosive oxygen burning that may occur in the near- M_{Ch} ONe core. We provided the initial parameter spaces for producing EC-SNe in the initial orbital period – initial He star mass ($\log P_{\text{orb}}^i - M_{\text{He}}^i$) diagram, and found that both M_{He}^i and minimum P_{orb}^i for EC-SNe increase with metallicity. Then, by considering NS kicks added to the newborn NS, we investigated the properties of the formed DNS systems after the He star companions collapse into NSs, such as the orbital periods, eccentricities and spin periods of recycle pulsars (P_{spin}), etc. The results show that most of the observed DNS systems can be produced by NS kicks of $\lesssim 50 \text{ km s}^{-1}$. In addition, we found that NSs could accrete more material if the residual H envelope on the He star companions is considered, which can form the mildly recycled pulsars ($P_{\text{spin}} \sim 20 \text{ ms}$) in DNS systems.

Key words: binaries: close – stars: evolution – pulsars: general – supernovae: general.

★ E-mail:yunlang@nju.edu.cn

† E-mail:wangbo@ynao.ac.cn

‡ E-mail:lixd@nju.edu.cn

1 INTRODUCTION

Electron-capture supernovae (EC-SNe) are induced by the e -capture on ^{24}Mg and ^{20}Ne in the strongly degenerate oxygen-neon (ONe) cores with masses close to the Chandrasekhar limit (M_{Ch} ; [Nomoto 1987](#)). It is generally suggested that the cores will eventually collapse into neutron stars (NSs) after undergoing EC-SNe (e.g. [Nomoto 1984](#); [Siess 2007](#); [Jones et al. 2013](#); [Doherty et al. 2015](#); [Tauris et al. 2015](#)). Because of the relatively steep density gradient in the outer cores, EC-SNe are expected to experience a prompt or fast explosion (see [Podsiadlowski et al. 2004](#)). Thus they may have relatively low explosion energies ($\sim 10^{50}$ erg, [Kitaura et al. 2006](#)), small amounts of ^{56}Ni ($\sim 0.002 - 0.015 M_{\odot}$, [Kitaura et al. 2006](#); [Wanajo et al. 2009](#)), and low-velocity kicks ($\lesssim 100 \text{ km s}^{-1}$, [Gessner & Janka 2018](#); [Stockinger et al. 2020](#)). In view of this, EC-SNe can explain a class of high-mass X-ray binaries with long orbital periods and low eccentricities, as well as the retention for NSs in globular clusters (e.g. [Pfahl et al. 2002](#); [Podsiadlowski et al. 2004](#)). Meanwhile, EC-SNe can be used to explain some low luminosity SNe, e.g. SNe 1997D ([Turatto et al. 1998](#)), SN 2005cs ([Pastorello et al. 2006, 2009](#)), SN 2008S ([Botticella et al. 2009](#)) and SN 2018zd ([Hiramatsu et al. 2021](#)). They are also potential sources for the r -process, which can synthesize heavy elements and contribute to the chemical evolution of galaxies ([Ning et al. 2007](#)). In addition, [Schwab et al. \(2010\)](#) studied the masses of 14 well-measured NSs, and found that the mass distribution of NSs may be bimodal, in which the lower mass peak ($\sim 1.25 M_{\odot}$) may arise from EC-SNe.

Double neutron star (DNS) systems are important potential gravitational wave sources, which can be formed in NS+He star systems after the He star companions undergo EC-SNe or iron core collapse supernovae (Fe CC-SNe; e.g. [Dewi et al. 2002](#); [Dewi & Pols 2003](#); [Ivanova et al. 2003](#); [Andrews et al. 2015](#); [Abbott et al. 2017](#); [Tauris et al. 2015, 2017](#); [Kruckow et al. 2018](#); [Jiang et al. 2021](#)). Since the discovery of the first DNS system decades ago (PSR B1913 + 16; [Hulse & Taylor 1975](#)), about 24 sources have been detected so far¹. The orbital periods of the observed DNS systems span a wide range from 0.1 d to 45.0 d, the orbital eccentricities range from 0.064 to 0.828, and the component masses mainly range from $1.1 - 1.5 M_{\odot}$. The observed features of DNSs are important for exploring their origin (e.g. [Tauris et al. 2017](#); [Shao & Li 2018](#); [Andrews & Mandel 2019](#)). It seems that most DNS systems are produced by small NS kick velocities, indicating that the EC-SN channel may provide an important contribution to the formation of DNS binaries. However, there are still some uncertainties for the origin of EC-SNe, although they play

¹ ATNF Pulsar Catalogue, <http://www.atnf.csiro.au/research/pulsar/psrcat> (version 1.71, November 2023; [Manchester et al. 2005](#))

a vital role in the formation of DNS binaries and the NS mass distribution in observations (e.g. [Tauris et al. 2015](#); [Jones et al. 2016](#); [Chanlaridis et al. 2022](#)).

Many works have been devoted to the study of the initial mass range for producing EC-SNe, which can be used in population synthesis studies (e.g. [Nomoto 1984](#); [Poelarends 2007](#); [Doherty et al. 2015](#); [Tauris et al. 2015](#); [Han et al. 2020](#)). It is generally believed that the initial masses of single main-sequence stars for producing EC-SNe are in the range of $\sim 8 - 10 M_{\odot}$ for solar metallicity, and this mass range is metallicity dependent (see e.g. [Doherty et al. 2017](#)). In the classic picture, the lower limit of metal core mass for producing EC-SNe is $\sim 1.37 M_{\odot}$ (e.g. [Nomoto 1984](#); [Takahashi et al. 2013](#)), and the upper limit of metal core mass is $\sim 1.43 M_{\odot}$ ([Tauris et al. 2015](#)). For the metal cores with masses less than $\sim 1.37 M_{\odot}$, stars will evolve into ONe white dwarfs (WDs). For the metal cores with masses larger than $\sim 1.43 M_{\odot}$, the stars will collapse into NSs through Fe CC-SNe. For the metal cores with masses of $1.37 - 1.43 M_{\odot}$, the oxygen deflagration is initiated in the center due to the heating of e -capture on ^{20}Ne . Subsequently, as the central temperature rises steeply, nuclear statistical equilibrium (NSE) will be achieved when temperature exceeds 5×10^9 K. The e -capture reactions in NSE region accelerate core contraction, resulting in the formation of NSs eventually if the e -capture rate exceeds the nuclear burning rate.

However, [Guo et al. \(2023, hereafter Paper I\)](#) recently found that explosive oxygen burning may be triggered after He stars develop ONe cores with masses close to M_{Ch} , and then the He stars may explode as Type Ia supernovae (SNe Ia) instead of collapsing into NSs (see also [Antoniadis et al. 2020](#); [Chanlaridis et al. 2022](#)). It is interesting to see how these new results affect the evolution of binary NSs resulting from EC-SNe. Accordingly, we will explore the formation of the EC-SNe in NS+He star binaries, and the properties of DNSs originating from the EC-SN channel. The basic method and assumptions for the binary evolution simulations are introduced in Section 2. The simulation results for EC-SNe in NS+He star binaries are presented in Section 3. We show the investigation of the properties of DNSs produced by EC-SNe in Section 4. Finally, we give discussions in Section 5 and a summary in Section 6.

2 NUMERICAL METHODS AND ASSUMPTIONS

We performed detailed binary evolution calculations of NS+He star systems by using the stellar evolution code Modules for Experiments in Stellar Astrophysics (MESA, version 10398; see [Paxton et al. 2018](#)), in which the initial NS mass (M_{NS}^i) is set to be $1.35 M_{\odot}$. Instead of solving the stellar structure equations of NSs, we assume that NSs to be point masses. In the present work, we

constructed zero-age main-sequence (ZAMS) He star models based on suite case create_zams. We mainly explored the parameter space for producing EC-SNe, where the initial He star mass (M_{He}^i) ranges from $\sim 2.4 M_{\odot}$ to $3.0 M_{\odot}$ with a resolution of $0.01 M_{\odot}$, and the initial orbital period (P_{orb}^i) ranges from ~ 0.07 d to 10 d with $\Delta \log P_{\text{orb}}^i = 0.5$.

During the binary evolution, the NS starts to accrete material from He star companion once the companion fills its Roche lobe. The scheme proposed by [Kolb & Ritter \(1990\)](#) is adopted to compute the mass-transfer rate (see also the Appendix in [Ge et al. 2010](#)), and the fraction of mass lost from the vicinity of the NS is set to be 0.5. Accordingly, the mass increase rate of NSs is $\dot{M}_{\text{NS}} = \min(0.5 \times \dot{M}_{\text{tran}}, \dot{M}_{\text{Edd}})$, in which $\dot{M}_{\text{Edd}} = 3 \times 10^{-8} M_{\odot} \text{ yr}^{-1}$ is the Eddington accretion rate and \dot{M}_{tran} is the mass-transfer rate (e.g. [Podsiadlowski et al. 2002](#); [Chen et al. 2020](#); [Wang et al. 2021](#)). In this work, the simulated mass-transfer rates are often 3 – 4 orders of magnitude larger than \dot{M}_{Edd} and therefore limited by \dot{M}_{Edd} (e.g. [Tauris et al. 2015](#); [Paper I](#)). We assume that the excess material ($\dot{M}_{\text{tran}} - \dot{M}_{\text{NS}}$) is ejected from the vicinity of the NS, carrying away the specific orbital angular momentum of the accreting NS (e.g. [Dewi et al. 2002](#); [Chen et al. 2011](#); [Wang et al. 2021](#); [Guo et al. 2022](#)).

During the evolution of He star companions, we adopted the ‘Dutch’ prescription with a scaling factor of 1.0 as the stellar wind mass-loss mechanism (e.g. [Glebbeek et al. 2009](#); [Antoniadis et al. 2020](#)). We used Type 2 Rosseland mean opacity tables provided by [Iglesias & Rogers \(1996\)](#), which can be applied to the enhanced carbon-oxygen caused by He-burning. The nuclear reaction network is coupled by 43 isotopes from ^1H – ^{58}Ni , including NeNa and MgAl cycles, Urca processes of $^{23}\text{Na} \rightleftharpoons ^{23}\text{Ne}$, $^{23}\text{Ne} \rightleftharpoons ^{23}\text{F}$, $^{25}\text{Mg} \rightleftharpoons ^{25}\text{Na}$ and $^{25}\text{Na} \rightleftharpoons ^{25}\text{Ne}$, and the e -capture chains, i.e. $^{24}\text{Mg}(e^-, \nu_e)^{24}\text{Na}(e^-, \nu_e)^{24}\text{Ne}$ and $^{20}\text{Ne}(e^-, \nu_e)^{20}\text{F}(e^-, \nu_e)^{20}\text{O}$. We used the weak interaction rates from [Suzuki et al. \(2016\)](#). In addition, we adopted the HELM and PC equations-of-state (e.g. [Timmes & Swesty 2000](#); [Potekhin & Chabrier 2010](#); [Schwab et al. 2017](#)).

In our simulations, we employed the Ledoux criterion and set the mixing-length parameter to be 2.0. We set the overshooting parameter (f_{ov}) to be 0.014 ([Jones et al. 2013](#); [Antoniadis et al. 2020](#)), and considered semi-convection ([Langer et al. 1983](#)) and thermohaline mixing ([Kippenhahn et al. 1980](#))². We stop the code if the e -capture on ^{20}Ne or the explosive oxygen burning occurs. For the models that can undergo Fe CC-SNe, the code is stopped after the formation of Si core.

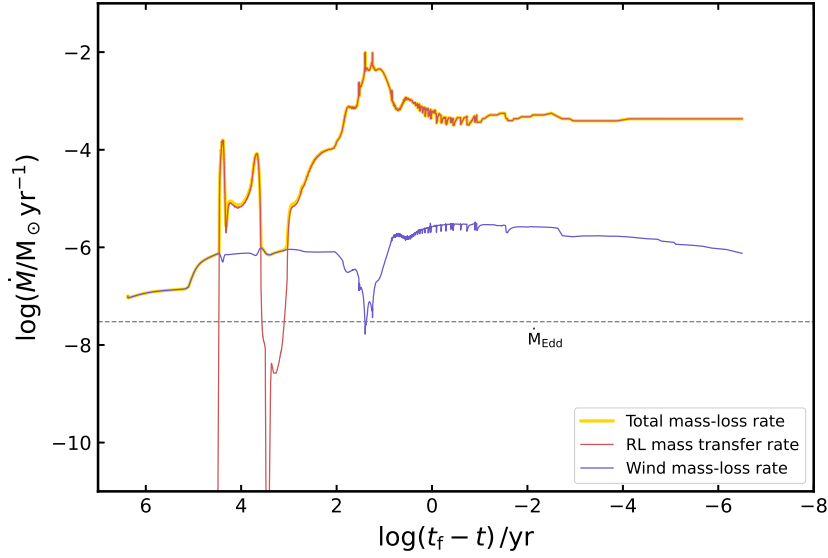


Figure 1. Mass-loss rate versus remaining time ($t_f - t$) for the $2.67 M_\odot$ He star companion, in which t and t_f are the stellar age and the total evolutionary time, respectively. The purple, red and yellow lines represent the stellar wind mass-loss rate, the mass-transfer rate and the total mass-loss rate, respectively. The dashed line indicates the Eddington accretion rate of the NS, i.e. $\dot{M}_{\text{Edd}} = 3 \times 10^{-8} M_\odot \text{yr}^{-1}$ for accretion of helium.

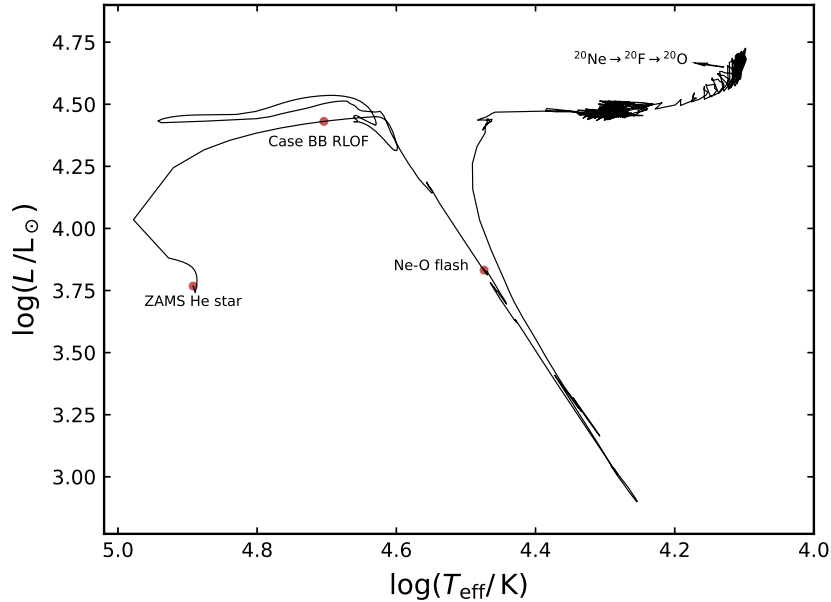


Figure 2. H-R diagram of a $2.67 M_\odot$ He star companion from He-ZAMS to e -capture on ^{20}Ne , in which the brown dots denote the moment when the He star evolution, the Case BB RLOF, the Ne-O flashes and the e -capture on ^{20}Ne begin.

3 RESULTS

3.1 Typical binary evolutionary example for EC-SNe

In Figs 1–4, we present an example of the evolution of a NS+He star binary with $M_{\text{He}}^i = 2.67 M_\odot$ and $P_{\text{orb}}^i = 1.0 \text{ d}$, in which the final fate of the He star companion is an EC-SN. Fig. 1 shows the evolution of mass-loss rate of He star companion as a function of remaining time ($t_f - t$) until

² The MESA inlists for this work are publicly available at https://zenodo.org/record/7655310#.Y_LaNS-KGx9.

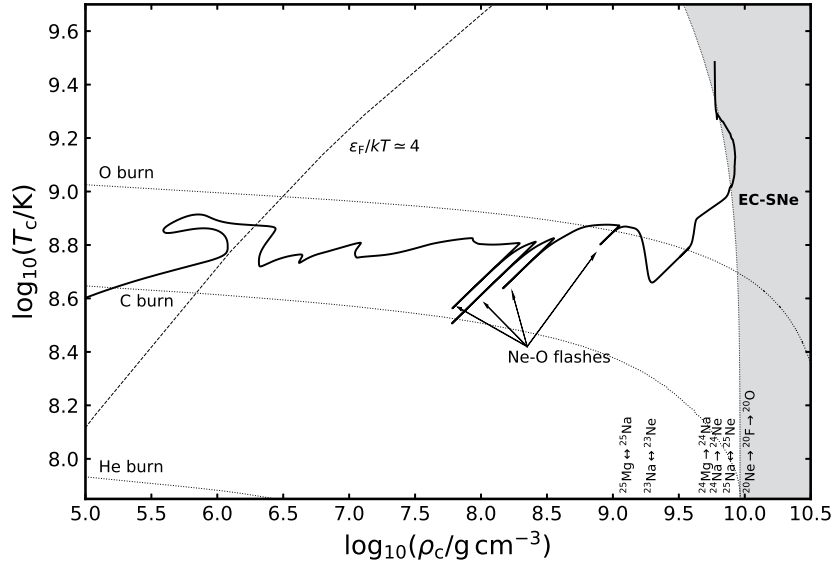


Figure 3. Central temperature versus central density for the $2.67 M_{\odot}$ He star companion. Grey shading denotes the region where the e -capture on ^{20}Ne occurs. The dotted lines represent helium, carbon and oxygen burning ignition curves, respectively. The dashed line denotes the separation of degenerate and non-degenerate regions ($\epsilon_F/kT \approx 4$).

e -capture on ^{20}Ne take place, where t and t_f are the stellar age and the total evolutionary time, respectively. The total simulated stellar age from He-ZAMS to e -capture is ~ 2.37 Myr. After the central helium exhaustion, the He star gradually expands, thereby leading to the initiation of Roche-lobe overflow (so-called Case BB RLOF) at $t \sim 2.35$ Myr. Fig. 2 shows the evolution of the companion in the H-R diagram. The points marked by the brown dots along the evolutionary track correspond to He star ZAMS, the onset of Case BB RLOF and other key processes. Fig. 3 illustrates the whole evolution of central temperature (T_c) and central density (ρ_c) for the He star companion.

Following central helium and carbon burning stage, the He star companion develops a $\sim 1.385 M_{\odot}$ ONe core which is surrounded by a $\sim 0.1 M_{\odot}$ He-layer. Fig. 4a shows the chemical structure of the mass donor after the carbon burning stage. At this moment, the ONe core is mainly composed of oxygen, neon, sodium and magnesium. Subsequently, neon is ignited off-center at mass coordinates (M_c) of $\sim 0.8 M_{\odot}$ due to the temperature inversion caused by the neutrino emission in the center of core (i.e. Ne-shell flash). From Fig. 3, it can be seen that the center reaches higher density and temperature after each Ne-shell flash quenches (Jones et al. 2013). Following a few Ne-shell flashes, the central density increases to $\log_{10}(\rho_c/\text{g cm}^{-3}) \approx 9.1$, resulting in the initiation of Urca processes. The central temperature decreases because of the Urca reactions. Meanwhile, the Urca reactions accelerate the contraction of the metal core, thereby leading to higher central density.

As the central density gradually increases, e -capture on ^{24}Mg and ^{20}Ne take place at $\log_{10}(\rho_c/\text{g cm}^{-3}) \approx 9.6$ and $\log_{10}(\rho_c/\text{g cm}^{-3}) \approx 9.9$, respectively (see Fig. 3). Fig. 4b shows the chemical structure of

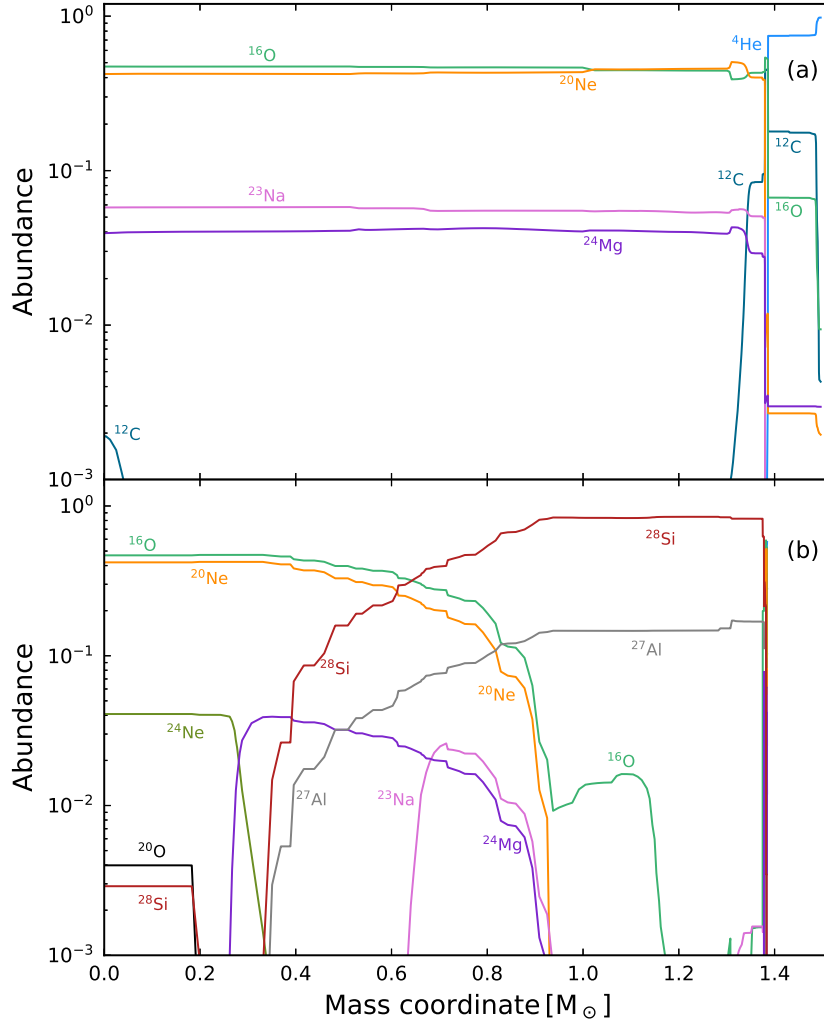


Figure 4. Panel (a): the chemical structure of the donor after carbon burning stage. At this moment, the donor mass is $\sim 1.50 M_{\odot}$, and the donor consists a $\sim 1.385 M_{\odot}$ ONe core and a $\sim 0.115 M_{\odot}$ He envelope. Panel (b): the chemical structure of the donor when the e -capture reactions on ^{20}Ne occur. At this moment, the donor consists of an ONe core and a thick Si shell.

the mass donor when the e -capture on ^{20}Ne occurs. We can see that the isotope ^{20}O is produced in the center owing to the reactions of $^{20}\text{Ne}(e^-, \nu_e)^{20}\text{F}(e^-, \nu_e)^{20}\text{O}$. Meanwhile, a thick Si-rich mantle is formed because of the Ne-shell flashes. At this moment, the final mass of the He envelope is $\sim 8.2 \times 10^{-4} M_{\odot}$, thus the He lines are not visible in the spectra after the core-collapse event (Hachinger et al. 2012).

3.2 Parameter space for EC-SNe

By calculating a large number of NS+He star systems with different M_{He}^i and P_{orb}^i , we obtained the initial contours for producing EC-SNe. Table 1 lists the information about the evolution of NS+He star binaries ($Z = 0.02$) at the boundaries of the parameter space for EC-SNe, in which the selected models correspond to the lowest simulated masses (for the given initial orbital period) to

Table 1. Evolutionary properties of the NS+He star binaries ($Z = 0.02$) at boundaries of the parameter space for EC-SNe, where the selected models correspond to the lowest simulated masses (for the given initial orbital period) to produce either Fe CC-SNe or EC-SNe. M_{He}^i and $\log P_{\text{orb}}^i$ are the initial mass of the He star companion and the initial orbital period; $M_{\text{core},f}$ and $M_{\text{env},f}$ are the final metal core mass and the remaining helium envelope mass of the donor prior to SN; ΔM_{NS} is the accreted mass of NS; $P_{\text{spin}}^{\text{min}}$ is the minimum spin period of NS; $P_{\text{orb}}^{\text{pre}}$ is the final orbital period prior to SN; t_f is the total evolution time of He star companion; the last column is the evolutionary outcome of the He star companion.

Set	M_{He}^i (M_{\odot})	$\log P_{\text{orb}}^i$ (d)	$M_{\text{core},f}$ (M_{\odot})	$M_{\text{env},f}$ (M_{\odot})	ΔM_{NS} (M_{\odot})	$P_{\text{spin}}^{\text{min}}$ (ms)	$P_{\text{orb}}^{\text{pre}}$ (d)	t_f (Myr)	Final fate
1	2.95	-1.15	1.431	4.5e-3	1.8e-3	38.7	0.069	2.02	Fe CC-SN
2	2.84	-1.15	1.381	3.0e-4	2.0e-3	36.0	0.075	2.14	EC-SN
3	2.88	-1.00	1.431	3.0e-3	1.6e-3	43.3	0.107	2.10	Fe CC-SN
4	2.79	-1.00	1.389	5.0e-4	1.7e-3	40.6	0.113	2.20	EC-SN
7	2.78	-0.50	1.430	4.7e-3	9.0e-4	65.7	0.361	2.22	Fe CC-SN
6	2.70	-0.50	1.396	7.3e-4	8.7e-4	67.1	0.378	2.32	EC-SN
7	2.77	0	1.436	3.0e-3	7.1e-4	78.2	1.153	2.23	Fe CC-SN
8	2.67	0	1.385	6.3e-4	8.2e-4	70.2	1.226	2.37	EC-SN
9	2.76	0.5	1.435	5.4e-3	5.7e-4	92.2	3.676	2.25	Fe CC-SN
10	2.65	0.5	1.383	4.5e-4	6.7e-4	81.6	3.915	2.40	EC-SN
11	2.76	1	1.433	6.4e-3	3.3e-4	138.3	11.65	2.25	Fe CC-SN
12	2.66	1	1.384	2.5e-4	4.8e-4	104.8	12.39	2.38	EC-SN
13 ^a	2.73	-1.15	1.433	1.6e-3	2.0e-3	36.8	0.057	2.23	Fe CC-SN
14 ^a	2.64	-1.15	1.385	4.2e-4	2.1e-3	34.2	0.062	2.35	EC-SN
15 ^a	2.54	1	1.443	1.7e-2	2.0e-4	208.5	9.502	2.56	Fe CC-SN
16 ^a	2.49	1	1.393	7.0e-4	3.0e-4	157.1	10.10	2.66	EC-SN

^a Models with a stellar wind efficiency of 0.1.

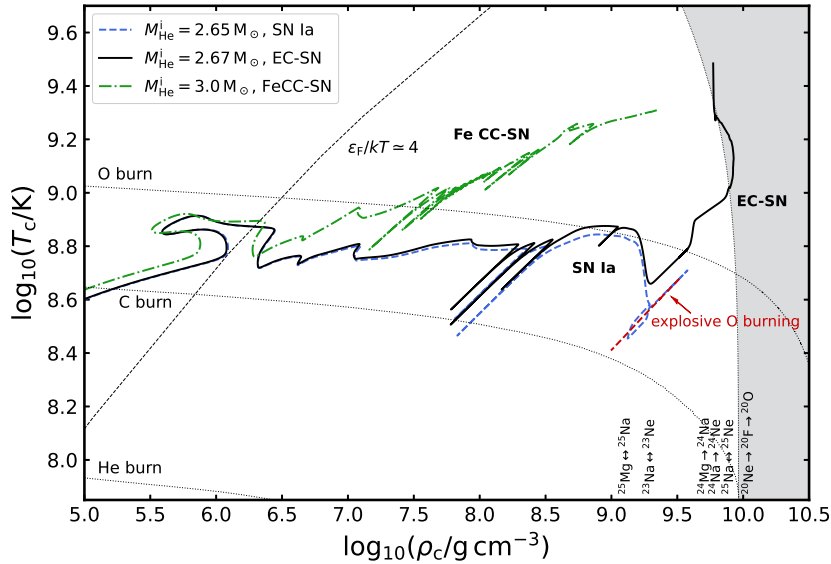


Figure 5. Evolutionary track of the central temperature and the central density for NS+naked He star binaries with different initial He star masses (i.e. $M_{\text{He}}^i = 2.65, 2.67$ and $3.0 M_{\odot}$), in which the initial orbital period of all models is 1.0 d.

produce either Fe CC-SNe or EC-SNe. The metal core mass for EC-SNe ranges from $\sim 1.385 M_{\odot}$ to $1.43 M_{\odot}$. If the final core mass is lower than $\sim 1.385 M_{\odot}$, then the explosive oxygen burning can be triggered owing to the convective Urca process, resulting in that the He star companions

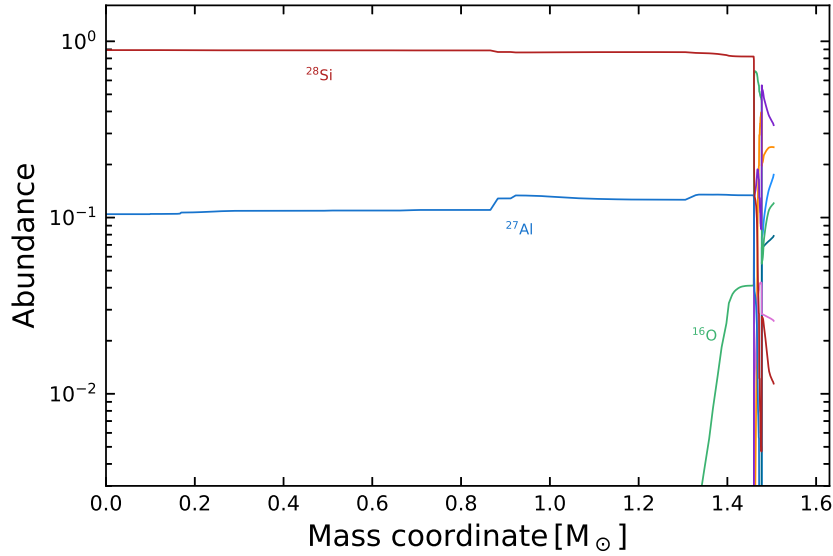


Figure 6. Final chemical structure for the He star companion with initial mass of $3.0 M_{\odot}$, in which the final core mass is $\sim 1.55 M_{\odot}$ and its final fate is an Fe CC-SN.

explode as SNe Ia eventually (see [Paper I](#)). If the final core mass is larger than $\sim 1.43 M_{\odot}$, then the final fates of He star companions are Fe CC-SNe.

Fig. 5 shows T_c versus ρ_c for three representative NS+He star binaries which terminate their evolution as an SN Ia, an EC-SN and an Fe CC-SN, respectively. For the model with $M_{\text{He}}^i = 2.65 M_{\odot}$, the He star companion develops a $\sim 1.378 M_{\odot}$ ONe core, and the explosive oxygen burning takes place owing to the convective Urca process, resulting in the formation of an SN Ia (see [Paper I](#)). For the model with $M_{\text{He}}^i = 2.67 M_{\odot}$, the He star companion develops a $\sim 1.385 M_{\odot}$ ONe core, and the He star will undergo EC-SN after e -capture on ^{20}Ne occurs. For the model with $M_{\text{He}}^i = 3.0 M_{\odot}$, the He star companion develops a $\sim 1.55 M_{\odot}$ ONe core, and the Ne-shell flash takes place at $M_c \approx 0.3 M_{\odot}$, which is closer to the center than the model with a $2.67 M_{\odot}$ He star companion. Fig. 6 shows the final chemical structure of the He star companion. The Ne-O burning flame can propagate to the center, leading to the formation of a silicon core, and thereby an iron core-collapse.

Fig. 7 represents the initial parameter spaces for EC-SNe in the $\log P_{\text{orb}}^i - M_{\text{He}}^i$ diagram with two metallicities (i.e. $Z = 0.0001, 0.02$), from which the metallicity has a strong influence on the parameter spaces. The left boundaries of the parameter spaces are set by the condition that RLOF takes place when the He star companions are on He-ZAMS stage. If the initial orbital period is $\gtrsim 10$ d, then the He star companions have a similar final fate. The dashed lines represent the boundaries between EC-SNe and Fe CC-SNe, and the solid lines represent the boundaries between SNe Ia and EC-SNe. We found that for a lower metallicity, the parameter spaces shifted to low-mass

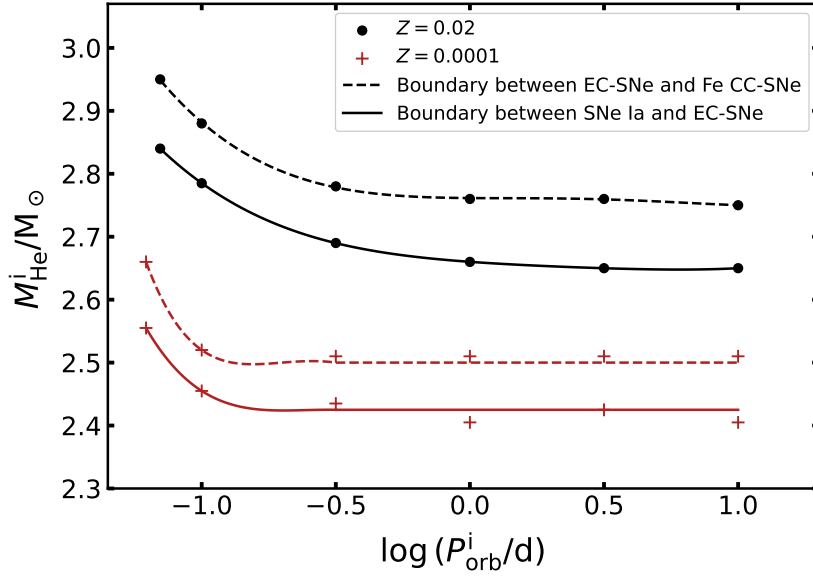


Figure 7. Initial parameter spaces in the $\log P_{\text{orb}}^i - M_{\text{He}}^i$ plane for NS+naked He star binaries that can produce EC-SNe. The dashed lines represent the boundaries between EC-SNe and Fe CC-SNe, and the solid lines represent the boundaries between SNe Ia and EC-SNe.

He star companion. This is because lower metallicities result in weaker stellar wind mass-loss and larger metal core for a given initial He star mass (e.g. [Chanlaridis et al. 2022](#); [Aguilera-Dena et al. 2022](#)). Meanwhile, lower metallicities lead to smaller radii of He ZAMS stars, thus the left boundaries of the parameter space shifts slightly to shorter initial period (see also [Wang & Han 2010](#)).

4 DOUBLE NEUTRON STAR SYSTEMS

The simulations show that the He star companions in NS binaries may explode as SNe Ia if the degenerate ONe core masses range from $\sim 1.335 - 1.385 M_{\odot}$ (see [Paper I](#)). Meanwhile, the NSs spin up during the mass-accretion phase, resulting in the formation of isolated mildly recycled pulsars after the He star companions experience SN Ia explosions. If the ONe core masses are larger than $\sim 1.385 M_{\odot}$, then the He star companions collapse into NSs through EC-SNe or Fe CC-SNe, which may result in the formation of DNS systems (e.g. [Tauris et al. 2017](#); [Kruckow et al. 2018](#)). Accordingly, we will study the DNS systems originating from the EC-SN channel, and compare our calculation results with observations.

4.1 The effects of SN explosions

It has been suggested that the eccentricity (e) and the orbital period of NS binaries will be changed after the companion star undergoes a SN explosion, due to the sudden mass loss and the kick

velocity (V_k) added to the newly-born NS. The orientation of the NS kick velocity is controlled by two angles, i.e. the angle between V_k and the pre-SN orbital velocity ($0 \leq \theta \leq 180^\circ$), and the positional angle of V_k with respect to the orbital plane ($-180^\circ < \phi \leq 180^\circ$). Thus, the ratio of pre-SN orbital separation (a_0) to the post-SN orbital separation (a) can be given by (e.g. [Hills 1983](#); [Dewi & Pols 2003](#); [Shao & Li 2016](#))

$$\frac{a_0}{a} = 2 - \frac{M_0}{M_0 - \Delta M} (1 + \nu^2 + 2\nu \cos \theta), \quad (1)$$

where M_0 and ΔM are the pre-SN total mass, and the ejected mass from the exploding star, respectively. In addition, we defined $\nu = V_k/V_0$, in which V_0 is relative velocity between the two stars. The eccentricity after SN explosions can be written as

$$1 - e^2 = \frac{a_0}{a} \frac{M_0}{M_0 - \Delta M} [1 + 2\nu \cos \theta + \nu^2 (\cos^2 \theta + \sin^2 \theta \sin^2 \phi)]. \quad (2)$$

We assume that the NS mass is $1.35 M_\odot$. In our simulations, the final companion star mass prior to SN ranges from $\sim 1.385 M_\odot$ to $1.43 M_\odot$, thus we adopt an average value of $1.4 M_\odot$. Accordingly, the pre-SN total mass is $2.75 M_\odot$. The ejected mass for EC-SNe is still highly uncertain. Previous studies generally suggested that the collapse of these objects can produce small ejected mass from $0.01 - 0.2 M_\odot$ (e.g. [Timmes et al. 1996](#); [Kitauro et al. 2006](#); [Fryer et al. 2012](#)). In this work, the value of ΔM is set to be $0.08 M_\odot$ ([Shao & Li 2018](#)). The small value of ΔM means that the properties of post-SN binaries are dominated by the natal NS kicks. In addition, it has been suggested that EC-SNe may produce low NS kicks owing to the fast explosions and relatively low explosion energies, while the value of NS kicks is still under debate (e.g. [Podsiadlowski et al. 2004](#); [Kitauro et al. 2006](#); [Verbunt et al. 2017](#); [Janka 2017](#); [Gessner & Janka 2018](#); [Stockinger et al. 2020](#)). [Tauris et al. \(2015\)](#) suggested that the amount of ejecta is extremely small for EC-SNe and low-mass Fe CC-SNe, resulting in small NS kicks less than $\sim 10 \text{ km s}^{-1}$. In addition, simulations of EC-SNe show that the explosion energy is about 10^{50} erg , which leads to the kick velocities lower than $\sim 50 \text{ km s}^{-1}$ (e.g. [Kitauro et al. 2006](#); [Dessart et al. 2006](#); [Janka 2017](#)). Accordingly, we assume that $V_k \leq 50 \text{ km s}^{-1}$ for EC-SNe.

4.2 DNS systems in the $P_{\text{orb}} - e$ diagram

Fig. 8 shows the effect of NS kicks and pre-SN orbital period on the distribution of post-SN systems in the $P_{\text{orb}} - e$ diagram, where we performed 2000 cycles with randomly oriented NS kicks for each pre-SN system. Obviously, larger V_k and longer pre-SN orbital period easily lead to higher post-SN eccentricity and longer post-SN P_{orb} . We note that if the systems have short pre-SN P_{orb} ($\lesssim 1 \text{ d}$) and relatively low V_k , then the post-SN P_{orb} does not change significantly. Additionally, the binaries

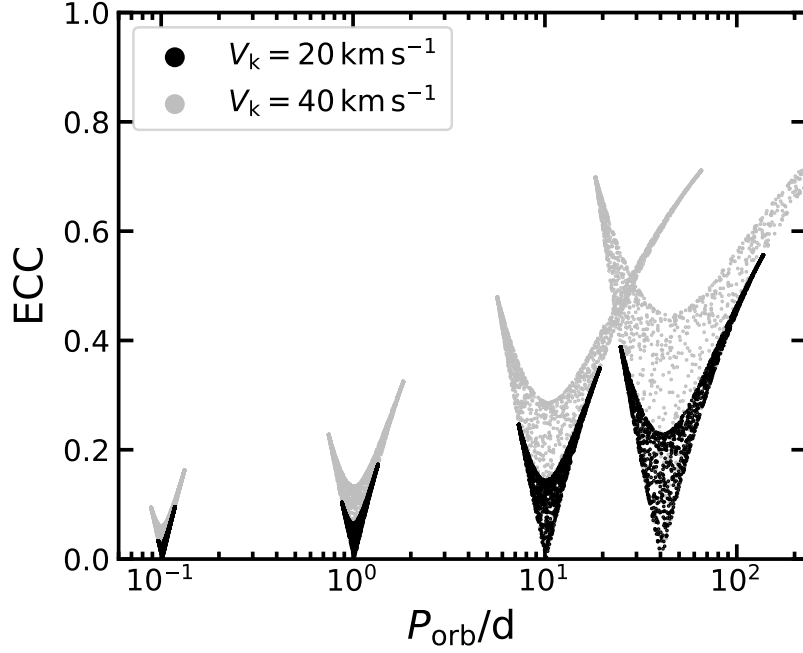


Figure 8. Distribution of the simulated post-SN systems in the $P_{\text{orb}} - e$ diagram, in which we performed 2000 cycles with randomly oriented NS kicks for each pre-SN system. We adopted four pre-SN orbital periods (i.e. 0.1, 1, 10 and 40 d) and two NS kicks (i.e. $V_k = 20$ and 40 km s^{-1}).

may be disrupted if they have wide-orbits. For example, if a pre-SN binary has parameters with $(V_k, P_{\text{orb}}) = (40 \text{ km s}^{-1}, 40 \text{ d})$, then the disruption probability for this system is 32%. Moreover, we found that the probability of the post-SN system located in the minimum and maximum period is relatively high, corresponding to θ around 180° and 0 , respectively.

Fig. 9 represents the distribution of the simulated post-SN systems in the $P_{\text{orb}} - e$ diagram, as well as the Galactic DNS systems in observations (red stars)³. We set 500 pre-SN P_{orb} that vary logarithmically from 0.07 d to 50 d, and each panel corresponds to different V_k , i.e. 10, 20, 30 and 50 km s^{-1} . We note that the post-SN systems are more likely to be located in the regions where the kick direction has a small impact on the $e - a$ relationship. Accordingly, we can conclude that lines I, II and III in Fig. 9 are the regions where post-SN systems are located with relatively high probability, corresponding to $\theta \sim 180^\circ$, $\theta \sim 0$ and $\phi \sim 0, \pm 180^\circ$, respectively. It can be seen that the NS kicks $\lesssim 50 \text{ km s}^{-1}$ could reproduce the most DNS systems, especially for the binaries with relatively low eccentricities. For example, PSR J1755 – 2550 (Ng et al. 2015) is a DNS candidate with a long orbital ($P_{\text{orb}} = 9.7 \text{ d}$) and a low eccentricity ($e = 0.09$). Ng et al. (2018) suggested that the minimum mass for the companion star of PSR J1755 – 2550 is $0.9 M_\odot$, but it is not completely determined whether the companion star is a NS or a WD. By assuming that PSR J1755 – 2550 is a DNS system, Tauris et al. (2017) suggested that this system may be formed by a NS kick lower

³ This probability distribution is not necessarily reflective of reality since we assume a uniform distribution of pre-SN $\log P_{\text{orb}}$.

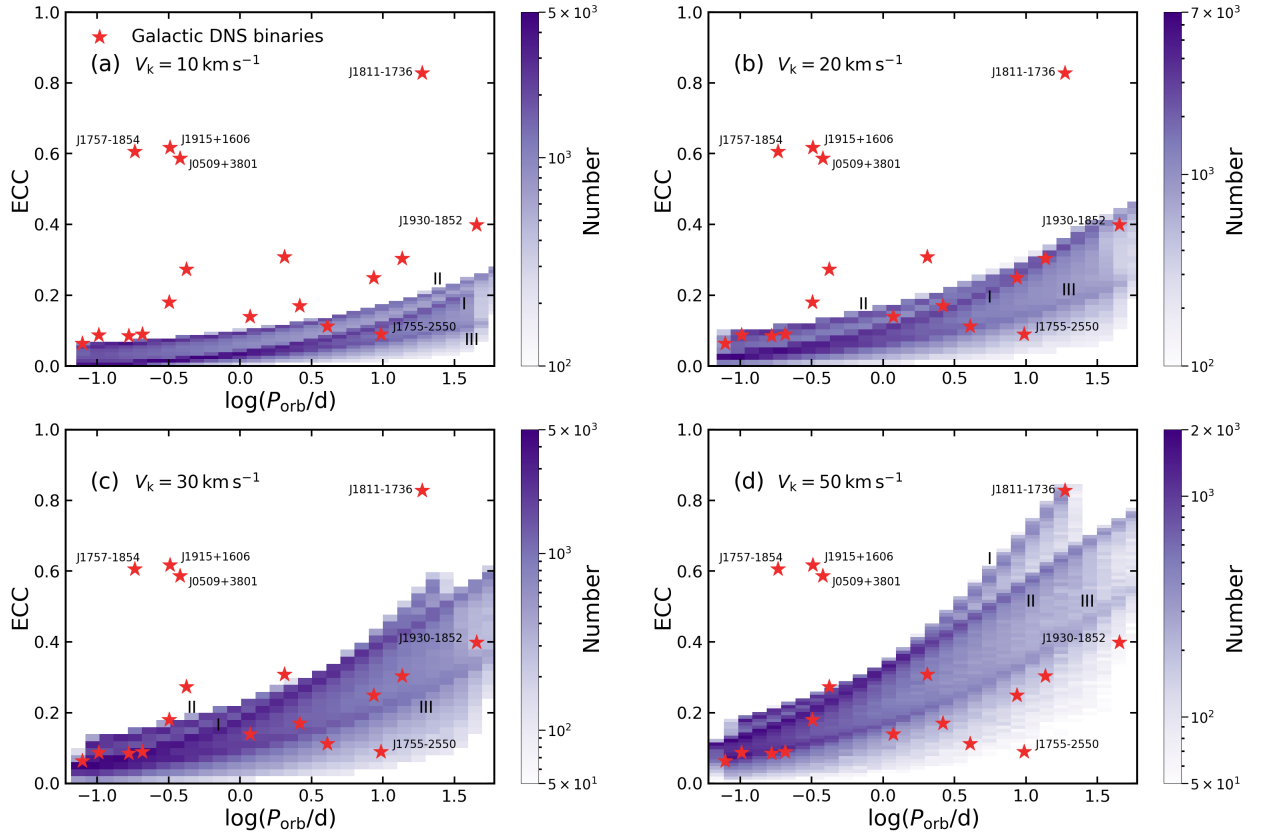


Figure 9. Distribution of the simulated post-SN systems in the $P_{\text{orb}} - e$ diagram (the purple regions), in which we set 500 pre-SN P_{orb} that vary logarithmically from 0.07 d to 50 d and the NS kicks are in the range of 10 – 50 km s^{-1} . We calculated 1000 cycles with randomly oriented NS kicks for each pre-SN system. Lines I, II and III are the regions where post-SN systems are located with relatively high probability, corresponding to $\theta \sim 180^\circ$, $\theta \sim 0$ and $\phi \sim 0, \pm 180^\circ$, respectively. The red stars are the Galactic DNS systems in observations. The observed data of DNS binaries are taken from the ATNF Pulsar Catalogue, <http://www.atnf.csiro.au/research/pulsar/psrcat> (version 1.71, November 2023; Manchester et al. 2005).

than 50 km s^{-1} . Our simulations also show that a NS kick of $\lesssim 30 \text{ km s}^{-1}$ (most likely $\sim 10 \text{ km s}^{-1}$) may explain the formation of PSR J1755 – 2550.

PSR J1930 – 1852 is the widest DNS system with a orbital period of 45 d (Swiggum et al. 2015). From Fig. 9, it is seen that its NS kick velocity was likely in the range of $\sim 20 - 50 \text{ km s}^{-1}$. PSR J1811 – 1736 has a long orbital period ($P_{\text{orb}} = 18.8 \text{ d}$) and the highest eccentricity ($e = 0.83$) among the known Galactic DNS systems (Corongiu et al. 2007). Although the results show that PSR J1811 – 1736 can be produced by kicks of $\sim 50 \text{ km s}^{-1}$, this source may come from different formation channel because of the huge gap at long periods and moderate eccentricities. In addition, kicks lower than $\sim 50 \text{ km s}^{-1}$ cannot account for three DNSs with high eccentricity, i.e. PSRs J0509 + 3801, J1757 – 1854 and J1915 + 1606. The distribution of the simulated post-SN systems for higher NS kick velocities are shown in Fig. A1. We can see that these three high eccentricity DNSs may originate from high NS kicks larger than $\sim 150 \text{ km s}^{-1}$ (see also Tauris et al. 2017).

Table 2. Properties of Galactic DNS systems. M_{total} , M_{psr} , M_{comp} are the binary total mass, the mass of radio pulsar and the mass of companion; P_{orb} , e , P_{spin} and \dot{P}_{spin} are the binary orbital period, the eccentricity of DNS system, the spin period of pulsar and its derivative; V_k and $P_{\text{orb}}^{\text{pre}}$ are the NS kick velocity and pre-SN orbital period estimated in this work.

	M_{total}	M_{psr}	M_{comp}	P_{orb}	e	P_{spin}	\dot{P}_{spin}	V_k	$P_{\text{orb}}^{\text{pre}}$
Pulsar name	(M_{\odot})	(M_{\odot})	(M_{\odot})	(d)		(ms)	(10^{-18})	(km s^{-1})	(d)
J0453 + 1559 ¹	2.734	1.559	1.174	4.072	0.113	45.8	0.186	$\lesssim 80$	$\sim 3 - 5$
J0509 + 3801 ²	2.805	1.348	1.468	0.380	0.586	76.5	80.54	$\gtrsim 150$	$\lesssim 0.9$
J0737 – 3039 ³	2.587	1.338	1.249	0.102	0.088	22.7	1.76	$\sim 20 - 200$	$\sim 0.08 - 0.1$
J1411 + 2551 ⁴	2.538	< 1.64	> 0.92	2.616	0.170	62.5	0.096	$\lesssim 100$	$\sim 2 - 4$
J1518 + 4904 ⁵	2.718	1.41	1.31	8.634	0.249	40.9	0.027	$\sim 20 - 80$	$\sim 4 - 15$
J1537 + 1155 ⁶	2.678	1.333	1.346	0.421	0.274	37.9	2.42	$\sim 30 - 200$	$\sim 0.2 - 0.7$
J1753 – 2240 ⁷	13.64	0.304	95.1	0.970	$\sim 20 - 80$	$\sim 7 - 20$
J1755 – 2550 ⁸	9.696	0.089	315	2434	$\lesssim 30$	$\sim 8 - 12$
J1756 – 2251 ⁹	2.569	1.341	1.230	0.320	0.181	28.5	1.018	$\sim 30 - 150$	$\sim 0.2 - 0.5$
J1757 – 1854 ¹⁰	2.733	1.338	1.395	0.184	0.606	21.5	2.630	$\gtrsim 150$	$\lesssim 0.3$
J1759 + 5036 ¹¹	2.62	< 1.92	> 0.70	2.043	0.308	176	0.243	$\sim 30 - 150$	$\sim 1 - 4$
J1811 – 1736 ¹²	2.57	< 1.75	> 0.91	18.78	0.828	104	0.901	$\sim 80 - 300$	$\sim 1 - 50$
J1829 + 2456 ¹³	2.59	< 1.38	> 1.22	1.176	0.139	41.0	0.053	$\sim 20 - 100$	$\sim 0.8 - 1.5$
J1906 + 0746 ¹⁴	2.613	1.291	1.322	0.166	0.085	144.1	20300	$\sim 20 - 150$	$\sim 0.13 - 0.2$
J1913 + 1102 ¹⁵	2.89	1.65	1.24	0.206	0.090	27.3	0.161	$\sim 20 - 150$	$\sim 0.15 - 0.3$
J1915 + 1606 ¹⁶	0.323	0.617	59.03	8.618	$\gtrsim 150$	$\lesssim 1.0$
J1930 – 1852 ¹⁷	45.06	0.400	185.5	19.00	$\sim 20 - 80$	$\sim 15 - 100$
J1946 + 2052 ¹⁸	2.50	< 1.35	> 1.17	0.078	0.064	17.0	0.92	$\lesssim 150$	$\sim 0.07 - 0.09$

References. 1: [Martinez et al. \(2015\)](#); 2: [Lynch et al. \(2018\)](#); 3: [Kramer et al. \(2006\)](#); 4: [Martinez et al. \(2017\)](#); 5: [Janssen et al. \(2008\)](#); 6: [Fonseca et al. \(2014\)](#); 7: [Keith et al. \(2009\)](#); 8: [Ng et al. \(2015\)](#); 9: [Ferdman et al. \(2014\)](#); 10: [Cameron et al. \(2018\)](#); 11: [Agazie et al. \(2021\)](#); 12: [Corongiu et al. \(2007\)](#); 13: [Champion et al. \(2005\)](#); 14: [van Leeuwen et al. \(2015\)](#); 15: [Ferdman & PALFA Collaboration \(2018\)](#); 16: [Weisberg et al. \(2010\)](#); 17: [Swiggum et al. \(2015\)](#); 18: [Stovall et al. \(2018\)](#).

4.3 Properties of pre-SN systems

Table 2 shows the properties of Galactic DNS systems, as well as their NS kick velocities and pre-SN orbital periods estimated in this work. We found that the DNSs with short orbital periods and high eccentricities (e.g. PSRs J0509 + 3801, J1757 – 1854 and J1915 + 1606) may be produced by high kick velocities (see also [Tauris et al. 2017](#)). However, it has been suggested that such systems may originate from other formation channel (see [Andrews & Mandel 2019](#), and discussion in Section 5.2). In addition, half of the DNSs have pre-SN orbital periods less than ~ 1 d and most DNSs may originate from the relatively low NS kicks. This may be caused by the selection effects, that is, the probability of surviving the pre-SN system is higher if it has a short orbital period or a low kick velocity. [Tauris et al. \(2017\)](#) calculated the probability of surviving the second SN in a binary with different pre-SN orbital periods and NS kicks. Their results indicate that for relatively tight systems with $P_{\text{orb}}^{\text{pre}} \lesssim 1$ d, all systems will survive if the NS kicks are lower than 100 km s^{-1} . Meanwhile, the orbital periods of such tight systems does not change significantly after the SN explosions, which is helpful for studying their pre-SN properties.

4.4 DNS systems in the $P_{\text{orb}} - P_{\text{spin}}$ diagram

4.4.1 The $P_{\text{orb}} - P_{\text{spin}}$ correlation

NSs in close X-ray binaries could be spun up during the mass-accretion process (e.g. [Alpar et al. 1982](#); [Bhattacharya & van den Heuvel 1991](#)), and the minimum spin period of the recycled pulsars can be expressed as ([Tauris et al. 2012](#))⁴:

$$P_{\text{spin}}^{\text{min}} \approx 0.34 \times (\Delta M_{\text{NS}}/M_{\odot})^{-3/4} \text{ ms}, \quad (3)$$

in which ΔM_{NS} is the accreted mass of NSs. For Case BB RLOF, the mass-transfer rate is much higher than \dot{M}_{Edd} (see Fig. 1), resulting in that most of the transferred material is ejected from the binaries and only a small amount of material are accreted by NS. From Table 1, we can see that the accreted masses of NSs range from $2.0 \times 10^{-4} M_{\odot}$ to $2.0 \times 10^{-3} M_{\odot}$, corresponding to initial orbital periods of 0.07 – 10 d. This results in the formation of recycled pulsars with $P_{\text{spin}}^{\text{min}} \sim 36 - 210$ ms after the He star companions undergo EC-SNe. Table 1 lists $P_{\text{spin}}^{\text{min}}$ and final orbital periods of NSs prior to EC-SNe, and their relation can be written as:

$$P_{\text{spin}}^{\text{min}} \approx 68 \pm 6 \text{ ms} \times (P_{\text{orb}}^{\text{pre}}/\text{d})^{0.22 \pm 0.05}. \quad (4)$$

In addition, longer $P_{\text{orb}}^{\text{i}}$ and larger M_{He}^{i} result in lower ΔM_{NS} , thereby leading to longer spin periods of the recycled pulsars (see also [Tauris et al. 2015](#)).

Fig. 10 represents the Galactic DNS systems (red stars) in the $P_{\text{orb}} - P_{\text{spin}}$ diagram. The black line indicates the relation between the simulated $P_{\text{spin}}^{\text{min}}$ and $P_{\text{orb}}^{\text{pre}}$ prior to SN (see Equation 4). From this figure, we can see that the DNSs with longer P_{orb} are preferentially accompanied by the recycled pulsars with higher P_{spin} , resulting from the shorter duration of the mass-accretion phase (e.g. [Tauris et al. 2015](#); [Paper I](#)). The brown shaded regions indicate the effect of NS kicks on the post-SN P_{orb} . As shown in this figure, longer $P_{\text{orb}}^{\text{pre}}$ and higher NS kicks will result in a wider range of the post-SN orbital periods. However, we note that this results hardly explain the DNS systems with relatively rapidly spinning recycled pulsars ($P_{\text{spin}} \lesssim 30$ ms). For example, the DNS system PSR J1946 + 2052 has a spin period of 17 ms, which is lower than the minimum value in our simulations (~ 38 ms, see Table 1). It has been suggested that such mildly recycled pulsars may be caused by the super-Eddington accretion, that is, Case BB RLOF allows first-born NS to accrete material at mass-accretion rates of 2 – 3 times \dot{M}_{Edd} (e.g. [Lazarus et al. 2014](#); [Tauris et al. 2017](#)).

⁴ The initial spin angular momentum can be negligible owing to the spin-down process during the detached stage with a timescale of $\sim 10^6$ yr. For example, the NS with an initial spin period of ~ 10 ms and a magnetic field of 10^{12} G spins down on a timescale of $\sim 10^4$ yr due to magnetic dipole radiation (see also equation 2 in [Kasen & Bildsten 2010](#)). In addition, the accretion will not play as significant a role if pulsars are already spinning at a high rate because pulsars have equilibrium periods.

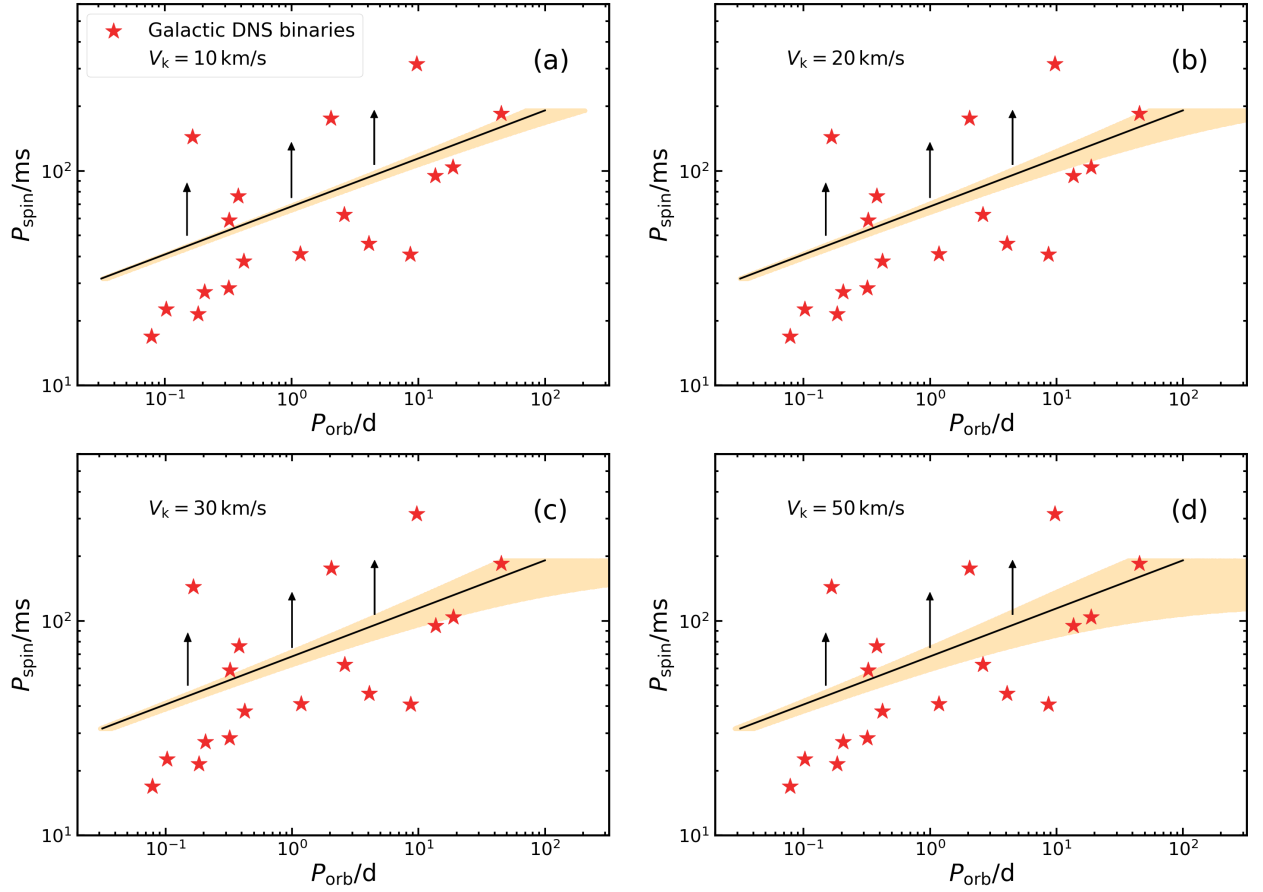


Figure 10. The $P_{\text{orb}} - P_{\text{spin}}$ diagram for the Galactic DNS systems (red stars) in observations. The black line (Equation 4) is a fit to our simulated results for the $(P_{\text{spin}}^{\text{min}}, P_{\text{orb}}^{\text{pre}})$ correlation, and the brown shaded regions represent the effect of the NS kick velocities on the post-SN P_{orb} .

In this work, we also provide a possible explanation for the relatively low spin period of pulsars by considering the residual H envelope on the surface of the He star companion, see Section 4.4.2.

4.4.2 The effect of residual H envelope on P_{spin}

It is generally believed that the NS+He star system that can form DNS has gone through the common envelope (CE) phase, in which the dynamic friction generated by the motion of NS inside the giant star’s envelope leads to the loss of orbital angular momentum and the ejection of the H-rich envelope (e.g. Paczynski 1976; Dewi & Pols 2003; Ivanova et al. 2013; Tauris et al. 2017). However, recent simulations suggest that a small amount of H shell still remains on the surface of He star companion after CE ejection (e.g. Fragos et al. 2019; Ge et al. 2022), which may affect the evolution of NS+He star systems. Accordingly, we calculated the evolution of three binaries taking into account the residual H envelope.

We evolved a $11 M_{\odot}$ MS star to the stage near the tip of red supergiant phase, where central helium burning has not yet occurred. We then removed the envelope until its radius less than the roche

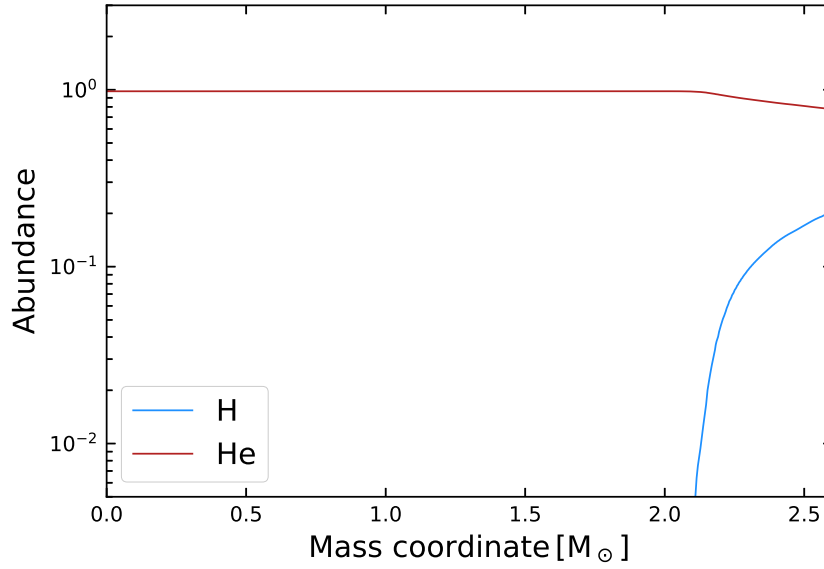


Figure 11. An example of the chemical structure of the He-ZAMS model with H envelope, where the total mass, He core mass and H envelope mass are $2.73 M_{\odot}$, $2.128 M_{\odot}$ and $0.598 M_{\odot}$, respectively.

lobe radius, e.g. for binary with $M_{\text{He}}^i \sim 2.7 M_{\odot}$ and $P_{\text{orb}}^i = 0.1$ d, the initial radius of companion star should be less than $\sim 0.63 R_{\odot}$. Meanwhile, the mass of the remaining H envelope should be in the range of $\sim 0.1 - 0.6 M_{\odot}$ (see, e.g. [Fragos et al. 2019](#)), consistent with the extended test of a $13 M_{\odot}$ primordial star based on [Ge et al. \(2022\)](#). After that, we put the He-ZAMS model with H envelope into the binary module to calculate the binary evolution. Fig. 11 shows an example of the chemical structure of the He star companion with H envelope. The He core mass and the H envelope mass are $\sim 2.13 M_{\odot}$ and $\sim 0.60 M_{\odot}$, in which the H abundance in the He core is assumed to be less than 0.01. Note that the outer layer is a mixture of H and He rather than a pure H shell. Table 3 lists evolutionary properties of three NS+He star binaries by considering the H envelope, as well as a binary system with a naked He star companion for comparison. We can see that the accreted mass of NS increases several times if the residual H envelope is assumed to remain on the surface of the He star companion. Meanwhile, the residual H envelope can also affect the final fate of the He star companion.

Fig. 12 shows the effect of the residual H envelope on the mass-transfer rate, in which the initial donor mass in both models is $2.73 M_{\odot}$ (see sets 18 and 20 in Table 3). The He star with a H envelope has a larger radius than the naked He star, causing it to fill its Roche lobe more easily. It can be seen that the H envelope results in a longer duration of the mass-transfer phase ([Bauer & Kupfer 2021](#)), thereby a larger accreted mass and a lower spin period of NS. Fig. 13 shows the theoretical (P_{orb} , P_{spin}) correlation calculated with and without the residual H envelope. The simulation results can better explain the observational characteristics of the DNS systems if we consider the H envelope on

Table 3. Characteristics of the binaries considering the residual H envelope on the surface of the He star companion, in which we set the stellar wind efficiency to be 0.1. M_{He}^i is the mass of the He-ZAMS model with H envelope; P_{orb}^i is the orbital period after the artificial stripping event; $M_{\text{He-core}}$, $M_{\text{H-env}}$ and $\log R^i$ are the initial He core mass, H envelope mass and the radius of the He star companion, respectively.

Set	M_{He}^i (M_{\odot})	$\log P_{\text{orb}}^i$ (d)	$M_{\text{He-core}}$ (M_{\odot})	$M_{\text{H-env}}$ (M_{\odot})	$\log R^i$ (R_{\odot})	$M_{\text{core,f}}$ (M_{\odot})	$M_{\text{env,f}}$ (M_{\odot})	ΔM_{NS} (M_{\odot})	$P_{\text{spin}}^{\text{min}}$ (ms)	P_{orb}^f (d)	t_f (Myr)	Final fate
17	2.66	-1.00	2.500	0.160	-0.20	1.386	1.2e-2	4.1e-3	21	0.088	2.25	EC-SN
18	2.73	0	2.128	0.598	0.42	1.388	1.0e-1	1.5e-3	45	0.833	2.66	EC-SN
19	2.72	1.00	2.125	0.595	0.36	1.470	3.8e-1	1.0e-3	60	7.701	2.46	Fe CC-SN
20	2.73	0	2.73	0	-0.37	1.513	2.5e-1	3.6e-4	130	0.780	2.30	Fe CC-SN

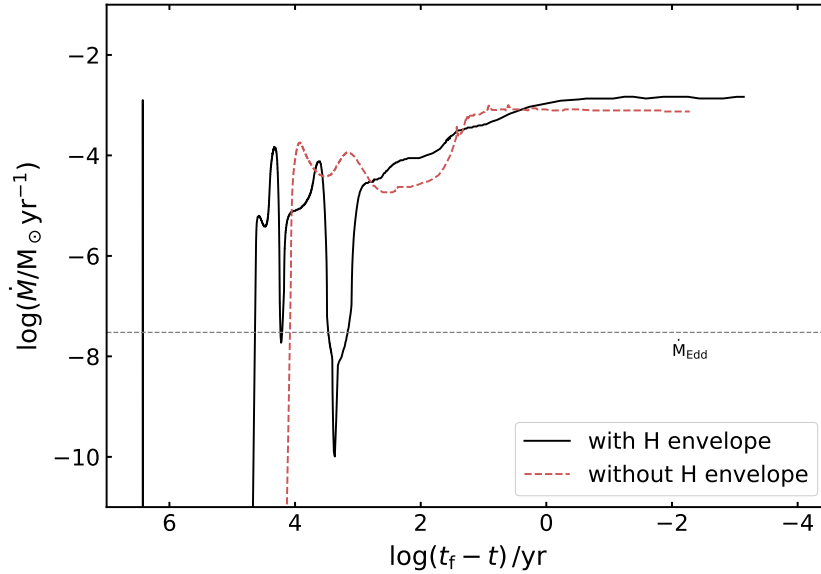


Figure 12. The effect of the H envelope on the mass-transfer rate, where the initial donor mass is $2.73 M_{\odot}$ (see sets 18 and 20 in Table 3). The black line and the red-dashed line denote the model considering the residual H envelope and the model with naked He star, respectively.

the surface of the He star companions. It is worth noting that the structure of the He star companion and the mass of the H envelope depend on the process of CE ejection. The impact of the residual H envelope on the evolution of pulsars needs to be systematically studied in future.

5 DISCUSSION

5.1 Uncertainties in the modelling

In our default models, we adopted the ‘Dutch’ stellar wind with a efficiency of 1.0 to calculate the wind mass-loss rate. However, different stellar wind efficiencies may change the evolutionary outcomes of the He stars. To further explore the influence of stellar wind efficiencies on the evolution of NS+He star systems, we computed four models with a stellar wind efficiency of 0.1 (see Table 1). The most significant effect is that lower wind efficiencies result in lower initial mass of the He star companion for EC-SNe. In addition, we note that the remaining helium envelope

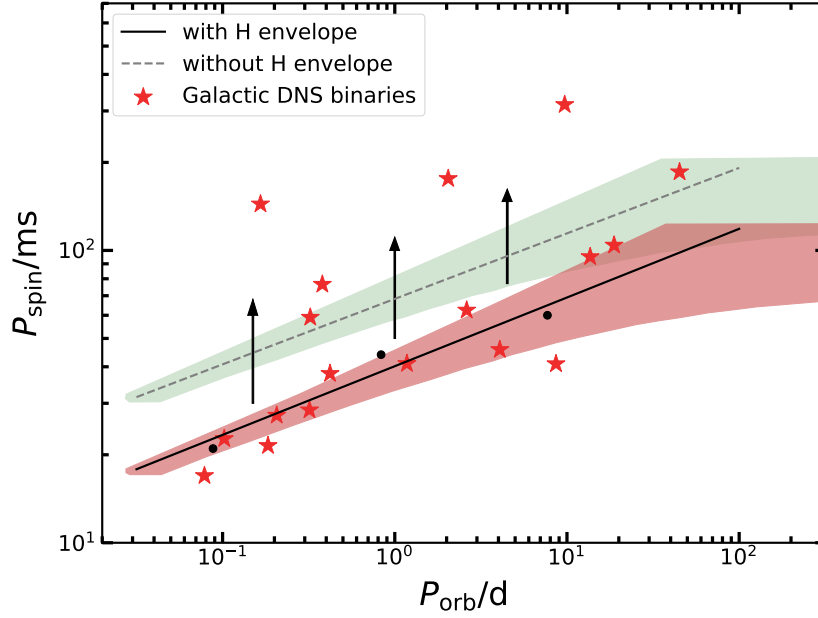


Figure 13. The $P_{\text{orb}} - P_{\text{spin}}$ diagram for the Galactic DNS systems (red stars) and our simulations. The black line and the gray dashed line represent the fitting results for the models with and without residual H envelope, respectively. The data of black dots come from sets 17 – 19 in Table 3. The green and red shaded regions represent the effect of the NS kick velocity ($V_k = 50 \text{ km s}^{-1}$).

mass ($M_{\text{He,f}}^{\text{env}}$) increases with the decrease of wind efficiency for the binaries with relatively long initial orbital periods, e.g. $P_{\text{orb}}^i = 10 \text{ d}$. However, the value of $M_{\text{He,f}}^{\text{env}}$ is still less than $0.06 M_{\odot}$ even though a low stellar wind efficiency is adopted, indicating that the EC-SN is likely to be classified as a Type Ic SN (Hachinger et al. 2012). In addition, convective overshooting is also an important physical process, which can result in higher effective temperature/luminosity, longer HeMS lifetime and a larger convective core (e.g. Yan et al. 2016; Chanlaridis et al. 2022). In the present work, we set the overshooting parameter to be 0.014 (e.g. Jones et al. 2013; Chanlaridis et al. 2022). We expect that the initial parameter space for EC-SNe will move up if a lower overshooting parameter is taken.

We assume that the ejected mass of the exploding star as $0.08 M_{\odot}$. However, by using the gravitational binding energy provided by Lattimer & Yahil (1989), Tauris et al. (2015) calculated the gravitational masses of the NS remnants, and found that about $0.2 M_{\odot}$ of the material could be ejected when the He star companions undergo EC-SNe. Accordingly, we calculated the distribution of post-SN systems in the $P_{\text{orb}} - e$ diagram by assuming the ejected mass as $0.2 M_{\odot}$ (see Fig. A2). We found that higher ejected mass leads to a wider range of eccentricity and the post-SN P_{orb} , although the influence is not significant. In addition, Tauris et al. (2017) suggested that post-SN simulations are also less dependent on the mass of the first-born NS.

5.2 Comparison to previous studies

[Tauris et al. \(2015\)](#) studied the parameter spaces for CO WDs, ONe WDs, EC-SNe and Fe CC-SNe in NS+He star systems. They assumed that EC-SNe will be produced if final metal core masses range from $1.37 M_{\odot}$ to $1.43 M_{\odot}$. However, our simulations show that the He star companions may explode as SNe Ia if the metal core masses range from $\sim 1.335 - 1.385 M_{\odot}$ ([Paper I](#)). This could result in a 25% reduction in the parameter space for producing EC-SNe. It has been suggested that the EC-SN channel mainly contributes to the formation of $\sim 1.24 - 1.29 M_{\odot}$ second-born NSs in DNSs (e.g. [Hüdepohl et al. 2010](#); [Kruckow et al. 2018](#)). [Kruckow et al. \(2018\)](#) studied the formation rate of DNSs by performing the binary population syntheses. From their Fig. 8, it can be seen that the final masses of second-born NSs range from $\sim 1.13 - 1.7 M_{\odot}$, and Fe CC-SN is the mainly channel for producing DNSs. Thus, the reduced EC-SN parameter space has no significant impact on the formation rate of DNSs.

By comparing with the results of [Tauris et al. \(2015\)](#), we note that the remaining helium envelope mass calculated in their study is larger than that of this work, and their simulations show that EC-SNe in some NS binaries may appear as ultra-stripped Type Ib SNe. This is because [Tauris et al. \(2015\)](#) stopped the code when the ONe cores are formed, while we continued the calculation to a later evolution stage, i.e. the e -capture on ^{20}Ne (see Fig. 4). We note that the donors still lose material at a rate of $\sim 10^{-4} - 10^{-3} M_{\odot} \text{ yr}^{-1}$ from ONe core formation to the e -capture on ^{20}Ne (see Fig. 1), which reduces the donor mass by $\sim 0.1 M_{\odot}$. Our simulations show that the final He envelope masses are lower than $0.06 M_{\odot}$ for NS+He star binaries with $P_{\text{orb}}^i \lesssim 10 \text{ d}$, and such EC-SNe may be observed as Type Ic SNe.

[Shao & Li \(2018\)](#) investigated the effect of the NS kicks on the distribution of DNS systems with population synthesis studies. They suggested that the second-born NSs in most DNS systems have kick velocities less than 80 km s^{-1} . [Tauris et al. \(2017\)](#) explored the pre-SN characters of DNS systems, and obtained the distribution of parameters of each source. Their results indicate that the kick velocity and pre-SN orbital period cover a wide range, and the peak values of kick velocities for most of the observed DNS systems tend to be less than $\sim 50 \text{ km s}^{-1}$ (see their Figs 24 – 38). Previous studies show that EC-SNe have explosion energies about $\sim 10^{50} \text{ erg}$ and low ejected mass between $0.01 - 0.2 M_{\odot}$ (e.g. [Kitaura et al. 2006](#); [Dessart et al. 2006](#); [Zha et al. 2022](#)), which may lead to the small NS kicks $\lesssim 50 \text{ km s}^{-1}$ or even $\lesssim 10 \text{ km s}^{-1}$ (e.g. [Janka 2017](#); [Tauris et al. 2017](#)). Meanwhile, our results show that the NS kick velocities of $\lesssim 50 \text{ km s}^{-1}$ can produce most observed DNS systems, indicating that EC-SNe may play an important role in the formation of DNSs.

[Janka \(2017\)](#) studied how the NS kick velocity depends on the explosion energy, ejecta mass, NS mass, and other relevant parameters. They found that massive metal cores tend to result in larger ejected masses and higher explosion energies, and therefore higher NS kick velocities. Meanwhile, [Tauris et al. \(2017\)](#) made statistics related to the masses of the second-born NSs and the kick velocities. They found that the second-born NSs with masses $\gtrsim 1.33 M_{\odot}$ are more likely to have high kick velocities, and suggested that smaller NS masses are preferentially accompanied by smaller NS kicks. Table 2 lists the NS kick velocities estimated from this work and the masses of the second-born NSs in observations. We also note that the DNS systems with high second-born NS masses may originate from high NS kicks (e.g. PSRs J0509 + 3801 and J1757 – 1854).

[Andrews & Mandel \(2019\)](#) divided the observed DNSs into three distinct subtypes according to the orbital characteristics: (1) DNSs with tight orbits and low eccentricities, which can merge within the Hubble time; (2) DNSs with wide orbits that cannot merge within the Hubble time; (3) DNSs with tight orbits and high eccentricities. Our theoretical results show that both subtypes (1) and (2) can be reproduced by the NS kicks $\lesssim 50 \text{ km s}^{-1}$. To explain the clustering of DNSs in subtype (3), i.e. PSRs J0509 + 3801, J1757 – 1854 and J1915 + 1606, [Andrews & Mandel \(2019\)](#) suggested that if the DNSs are the product of isolated binary evolution, then the second-born NSs must have a small natal kicks $\lesssim 25 \text{ km s}^{-1}$ and the pre-SN He star masses narrowly distributed around $3.2 M_{\odot}$. In addition, they also proposed that the DNSs in subtype (3) may originate from dynamical formation channel, that is, the DNSs firstly formed in globular cluster, and was then dynamically kicked into the Milky Way field (see [Phinney & Sigurdsson 1991](#)).

PSR J1952 + 2630 is a mildly recycled 20.7 ms pulsar orbiting together with a massive WD companion ($\gtrsim 0.93 M_{\odot}$), and its orbital period is 9.4 h ([Lazarus et al. 2014](#)). Such tight orbit indicates that this system has undergone CE evolution and form a NS+He star system, and then the NS spins up through the Case BB RLOF. [Lazarus et al. \(2014\)](#) suggested that the relatively fast spin of this pulsar may be caused by the super-Eddington accretion with mass-accretion rate between $\sim 100 - 300$ per cent of \dot{M}_{Edd} . According to our simulations, we concluded that such mildly recycled pulsar+WD systems can also be produced if the residual H envelope on the surface of He star companion is considered.

5.3 Thermonuclear EC-SNe

Previous studies usually assumed that the e -capture on ^{20}Ne takes place if ONe cores have masses $\gtrsim 1.37 M_{\odot}$, resulting in that the ONe cores collapse into NS through EC-SNe (e.g. [Nomoto](#)

1984; Tauris et al. 2015; Doherty et al. 2015). However, by performing the multidimensional hydrodynamic simulations for oxygen deflagration in ONe cores with three different central ignition densities, Jones et al. (2016) found that the ONe cores may not collapse into NSs if oxygen deflagration is triggered at ignition density $\log_{10}(\rho_c/\text{g cm}^{-3}) \lesssim 10$, while $\sim 0.1 - 1 M_\odot$ of material will be ejected and leave bound ONeFe WD remnants, called the thermonuclear EC-SNe (see also Isern et al. 1991; Kirsebom et al. 2019; Jones et al. 2019). On the other hand, the ONe cores will collapse into NSs at relatively high ignition density $\log_{10}(\rho_c/\text{g cm}^{-3}) \gtrsim 10$. Fig. 3 shows that the explosive oxygen burning occurs at central density of $\log_{10}(\rho_c/\text{g cm}^{-3}) \sim 9.8$, indicating that this NS+He star binaries may evolve into eccentric pulsar+WD systems after SN explosions.

PSR J0453 + 1559 is a DNS system candidate with $P_{\text{orb}} = 4.07 \text{ d}$ and $e = 0.1125$ (Martinez et al. 2015). The mass of the recycled pulsar and its companion are $1.559(5) M_\odot$ and $1.174(4) M_\odot$, respectively. However, it is unclear whether the companion is a NS or a WD. The mass of its companion is significantly lower than that of the second-born NSs in other DNS systems, indicating that the companion is more likely not a NS. On the other hand, the eccentricity of 0.1125 is high for normal NS+WD systems. In view of this, Tauris & Janka (2019) used the thermonuclear EC-SN channel to explain the formation of this system, and they found that PSR J0453 + 1559 may be produced by a kick velocity from $\sim 70 \text{ km s}^{-1}$ to 100 km s^{-1} . More numerical simulations and observations about thermonuclear EC-SNe are needed to verify this scenario.

6 SUMMARY

Using the stellar evolution code MESA, we systematically studied EC-SNe in NS+He star binaries with $P_{\text{orb}}^i < 10 \text{ d}$. In our simulations, the e -captures on ^{20}Ne are triggered if the He star companions develop highly degenerate ONe cores with masses from $\sim 1.385 M_\odot$ to $1.43 M_\odot$. SNe Ia are produced if the core masses $\lesssim 1.385 M_\odot$, owing to the explosive oxygen burning caused by the convective Urca process. The final fates of the He stars will be Fe CC-SNe if the core masses $\gtrsim 1.43 M_\odot$. We calculated a series of NS+He star binaries and obtained initial parameter spaces for producing EC-SNe in the $\log P_{\text{orb}}^i - M_{\text{He}}^i$ diagram, and found that higher metallicity can result in higher M_{He}^i and minimum P_{orb}^i for EC-SNe.

By considering the kicks added to the second-born NS, we then explored the properties of the formed DNS systems after the He star companions collapse into NSs through EC-SNe, such as the post-SN orbital period, eccentricity and the spin period of recycle pulsar, etc. Based on the comparison between numerical simulations and observations, we found that the majority of the

observed DNS systems can be explained by the NS kicks of $\lesssim 50 \text{ km s}^{-1}$, indicating that the EC-SN channel may play an important role in the formation of DNS systems. We also estimated the properties of the pre-SN systems of the observed DNS systems, and found that half of the observed DNS systems seem to have tight pre-SN orbit ($\lesssim 1 \text{ d}$), resulting from the higher probability of surviving post-SN systems. In addition, by assuming that the residual H envelope remains on the surface of the He star companion, we found that the first-born NSs could accrete enough material to form the mildly recycled pulsars ($P_{\text{spin}} \sim 20 \text{ ms}$) in DNS systems.

ACKNOWLEDGEMENTS

We thank the anonymous referee for valuable comments that help to improve the paper. This study is supported by the the National Natural Science Foundation of China (Nos 12041301, 12121003, 12225304, 12090040/12090043, 12273014, 12288102, 12125303, 12173081 and 11733009), National Key R&D Program of China (Nos 2021YFA0718500, 2021YFA1600404 and 2021YFA1600403), the Western Light Project of CAS (No. XBZG-ZDSYS-202117), the science research grant from the China Manned Space Project (No. CMS-CSST-2021-A12), the Yunnan Fundamental Research Project (Nos 202101AV070001 and 202201BC070003), the Frontier Scientific Research Program of Deep Space Exploration Laboratory (No. 2022-QYKYJH-ZYTS-016), the key research program of frontier sciences, CAS, No. ZDBS-LY-7005, and the Shandong Fundamental Research Project (No. ZR2021MA013). The authors also acknowledge the “PHOENIX Supercomputing Platform” jointly operated by the Binary Population Synthesis Group and the Stellar Astrophysics Group at Yunnan Observatories, Chinese Academy of Sciences.

DATA AVAILABILITY

Results will be shared on reasonable request to corresponding author.

REFERENCES

- Abbott B. P., et al., 2017, *Phys. Rev. Lett.*, 119, 161101
- Agazie G. Y., et al., 2021, *ApJ*, 922, 35
- Aguilera-Dena D. R., Müller B., Antoniadis J., Langer N., Dessart L., Vigna-Gómez A., Yoon S.-C., 2022, arXiv e-prints, p. [arXiv:2204.00025](https://arxiv.org/abs/2204.00025)
- Alpar M. A., Cheng A. F., Ruderman M. A., Shaham J., 1982, *Nature*, 300, 728
- Andrews J. J., Mandel I., 2019, *ApJ*, 880, L8
- Andrews J. J., Farr W. M., Kalogera V., Willems B., 2015, *ApJ*, 801, 32
- Antoniadis J., Chanlaridis S., Gräfenor G., Langer N., 2020, *A&A*, 635, A72
- Bauer E. B., Kupfer T., 2021, *ApJ*, 922, 245

- Bhattacharya D., van den Heuvel E. P. J., 1991, *Phys. Rep.*, **203**, 1
- Botticella M. T., et al., 2009, *MNRAS*, **398**, 1041
- Cameron A. D., et al., 2018, *MNRAS*, **475**, L57
- Champion D. J., et al., 2005, *MNRAS*, **363**, 929
- Chanlaridis S., Antoniadis J., Aguilera-Dena D. R., Gräfenor G., Langer N., Stergioulas N., 2022, *A&A*, **668**, A106
- Chen W. C., Li X. D., Xu R. X., 2011, *A&A*, **530**, A104
- Chen W.-C., Liu D.-D., Wang B., 2020, *ApJ*, **900**, L8
- Corongiu A., Kramer M., Stappers B. W., Lyne A. G., Jessner A., Possenti A., D’Amico N., Löhmer O., 2007, *A&A*, **462**, 703
- Dessart L., Burrows A., Ott C. D., Livne E., Yoon S. C., Langer N., 2006, *ApJ*, **644**, 1063
- Dewi J. D. M., Pols O. R., 2003, *MNRAS*, **344**, 629
- Dewi J. D. M., Pols O. R., Savonije G. J., van den Heuvel E. P. J., 2002, *MNRAS*, **331**, 1027
- Doherty C. L., Gil-Pons P., Siess L., Lattanzio J. C., Lau H. H. B., 2015, *MNRAS*, **446**, 2599
- Doherty C. L., Gil-Pons P., Siess L., Lattanzio J. C., 2017, *Publ. Astron. Soc. Australia*, **34**, e056
- Ferdman R. D., PALFA Collaboration 2018, in Weltevrede P., Perera B. B. P., Preston L. L., Sanidas S., eds, Vol. 337, *Pulsar Astrophysics the Next Fifty Years*. pp 146–149, doi:10.1017/S1743921317009139
- Ferdman R. D., et al., 2014, *MNRAS*, **443**, 2183
- Fonseca E., Stairs I. H., Thorsett S. E., 2014, *ApJ*, **787**, 82
- Fragos T., Andrews J. J., Ramirez-Ruiz E., Meynet G., Kalogera V., Taam R. E., Zezas A., 2019, *ApJ*, **883**, L45
- Fryer C. L., Belczynski K., Wiktorowicz G., Dominik M., Kalogera V., Holz D. E., 2012, *ApJ*, **749**, 91
- Ge H., Hjellming M. S., Webbink R. F., Chen X., Han Z., 2010, *ApJ*, **717**, 724
- Ge H., et al., 2022, *ApJ*, **933**, 137
- Gessner A., Janka H.-T., 2018, *ApJ*, **865**, 61
- Glebbeek E., Gaburov E., de Mink S. E., Pols O. R., Portegies Zwart S. F., 2009, *A&A*, **497**, 255
- Guo Y.-L., Wang B., Han Z.-W., 2022, *MNRAS*, **515**, 2725
- Guo Y.-L., Wang B., Wu C.-Y., Chen W.-C., Jiang L., Han Z.-W., 2023, *MNRAS*, **526**, 932
- Hachinger S., Mazzali P. A., Taubenberger S., Hillebrandt W., Nomoto K., Sauer D. N., 2012, *MNRAS*, **422**, 70
- Han Z.-W., Ge H.-W., Chen X.-F., Chen H.-L., 2020, *Research in Astronomy and Astrophysics*, **20**, 161
- Hills J. G., 1983, *ApJ*, **267**, 322
- Hiramatsu D., et al., 2021, *Nature Astronomy*, **5**, 903
- Hüdepohl L., Müller B., Janka H. T., Marek A., Raffelt G. G., 2010, *Phys. Rev. Lett.*, **104**, 251101
- Hulse R. A., Taylor J. H., 1975, *ApJ*, **195**, L51
- Iglesias C. A., Rogers F. J., 1996, *ApJ*, **464**, 943
- Isern J., Canal R., Labay J., 1991, *ApJ*, **372**, L83
- Ivanova N., Belczynski K., Kalogera V., Rasio F. A., Taam R. E., 2003, *ApJ*, **592**, 475
- Ivanova N., et al., 2013, *A&ARv*, **21**, 59
- Janka H.-T., 2017, *ApJ*, **837**, 84
- Janssen G. H., Stappers B. W., Kramer M., Nice D. J., Jessner A., Cognard I., Purver M. B., 2008, *A&A*, **490**, 753
- Jiang L., Tauris T. M., Chen W.-C., Fuller J., 2021, *ApJ*, **920**, L36
- Jones S., et al., 2013, *ApJ*, **772**, 150
- Jones S., Röpke F. K., Pakmor R., Seitzzahl I. R., Ohlmann S. T., Edelmann P. V. F., 2016, *A&A*, **593**, A72
- Jones S., et al., 2019, *A&A*, **622**, A74
- Kasen D., Bildsten L., 2010, *ApJ*, **717**, 245
- Keith M. J., Kramer M., Lyne A. G., Eatough R. P., Stairs I. H., Possenti A., Camilo F., Manchester R. N., 2009, *MNRAS*, **393**, 623
- Kippenhahn R., Ruschenplatt G., Thomas H. C., 1980, *A&A*, **91**, 175
- Kirsebom O. S., et al., 2019, *Phys. Rev. Lett.*, **123**, 262701

- Kitaura F. S., Janka H. T., Hillebrandt W., 2006, *A&A*, **450**, 345
- Kolb U., Ritter H., 1990, *A&A*, **236**, 385
- Kramer M., et al., 2006, *Science*, **314**, 97
- Kruckow M. U., Tauris T. M., Langer N., Kramer M., Izzard R. G., 2018, *MNRAS*, **481**, 1908
- Langer N., Fricke K. J., Sugimoto D., 1983, *A&A*, **126**, 207
- Lattimer J. M., Yahil A., 1989, *ApJ*, **340**, 426
- Lazarus P., et al., 2014, *MNRAS*, **437**, 1485
- Lynch R. S., et al., 2018, *ApJ*, **859**, 93
- Manchester R. N., Hobbs G. B., Teoh A., Hobbs M., 2005, *AJ*, **129**, 1993
- Martinez J. G., et al., 2015, *ApJ*, **812**, 143
- Martinez J. G., et al., 2017, *ApJ*, **851**, L29
- Ng C., et al., 2015, *MNRAS*, **450**, 2922
- Ng C., et al., 2018, *MNRAS*, **476**, 4315
- Ning H., Qian Y. Z., Meyer B. S., 2007, *ApJ*, **667**, L159
- Nomoto K., 1984, *ApJ*, **277**, 791
- Nomoto K., 1987, *ApJ*, **322**, 206
- Paczynski B., 1976, in Eggleton P., Mitton S., Whelan J., eds, Vol. 73, Structure and Evolution of Close Binary Systems. p. 75
- Pastorello A., et al., 2006, *MNRAS*, **370**, 1752
- Pastorello A., et al., 2009, *MNRAS*, **394**, 2266
- Paxton B., et al., 2018, *ApJS*, **234**, 34
- Pfahl E., Rappaport S., Podsiadlowski P., 2002, *ApJ*, **573**, 283
- Phinney E. S., Sigurdsson S., 1991, *Nature*, **349**, 220
- Podsiadlowski P., Rappaport S., Pfahl E. D., 2002, *ApJ*, **565**, 1107
- Podsiadlowski P., Langer N., Poelarends A. J. T., Rappaport S., Heger A., Pfahl E., 2004, *ApJ*, **612**, 1044
- Poelarends A. J. T., 2007, PhD thesis, University of Utrecht, Netherlands
- Potekhin A. Y., Chabrier G., 2010, *Contributions to Plasma Physics*, **50**, 82
- Schwab J., Podsiadlowski P., Rappaport S., 2010, *ApJ*, **719**, 722
- Schwab J., Bildsten L., Quataert E., 2017, *MNRAS*, **472**, 3390
- Shao Y., Li X.-D., 2016, *ApJ*, **816**, 45
- Shao Y., Li X.-D., 2018, *ApJ*, **867**, 124
- Siess L., 2007, *A&A*, **476**, 893
- Stockinger G., et al., 2020, *MNRAS*, **496**, 2039
- Stovall K., et al., 2018, *ApJ*, **854**, L22
- Suzuki T., Toki H., Nomoto K., 2016, *ApJ*, **817**, 163
- Swiggum J. K., et al., 2015, *ApJ*, **805**, 156
- Takahashi K., Yoshida T., Umeda H., 2013, *ApJ*, **771**, 28
- Tauris T. M., Janka H.-T., 2019, *ApJ*, **886**, L20
- Tauris T. M., Langer N., Kramer M., 2012, *MNRAS*, **425**, 1601
- Tauris T. M., Langer N., Podsiadlowski P., 2015, *MNRAS*, **451**, 2123
- Tauris T. M., et al., 2017, *ApJ*, **846**, 170
- Timmes F. X., Swesty F. D., 2000, *ApJS*, **126**, 501
- Timmes F. X., Woosley S. E., Weaver T. A., 1996, *ApJ*, **457**, 834
- Turatto M., et al., 1998, *ApJ*, **498**, L129
- Verbunt F., Igoshev A., Cator E., 2017, *A&A*, **608**, A57
- Wanajo S., Nomoto K., Janka H. T., Kitaura F. S., Müller B., 2009, *ApJ*, **695**, 208

- Wang B., Han Z., 2010, [A&A](#), **515**, A88
- Wang B., Chen W.-C., Liu D.-D., Chen H.-L., Wu C.-Y., Tang W.-S., Guo Y.-L., Han Z.-W., 2021, [MNRAS](#), **506**, 4654
- Weisberg J. M., Nice D. J., Taylor J. H., 2010, [ApJ](#), **722**, 1030
- Yan J.-Z., Zhu C.-H., Wang Z.-J., Lü G.-L., 2016, [Research in Astronomy and Astrophysics](#), **16**, 141
- Zha S., O'Connor E. P., Couch S. M., Leung S.-C., Nomoto K., 2022, [MNRAS](#), **513**, 1317
- van Leeuwen J., et al., 2015, [ApJ](#), **798**, 118

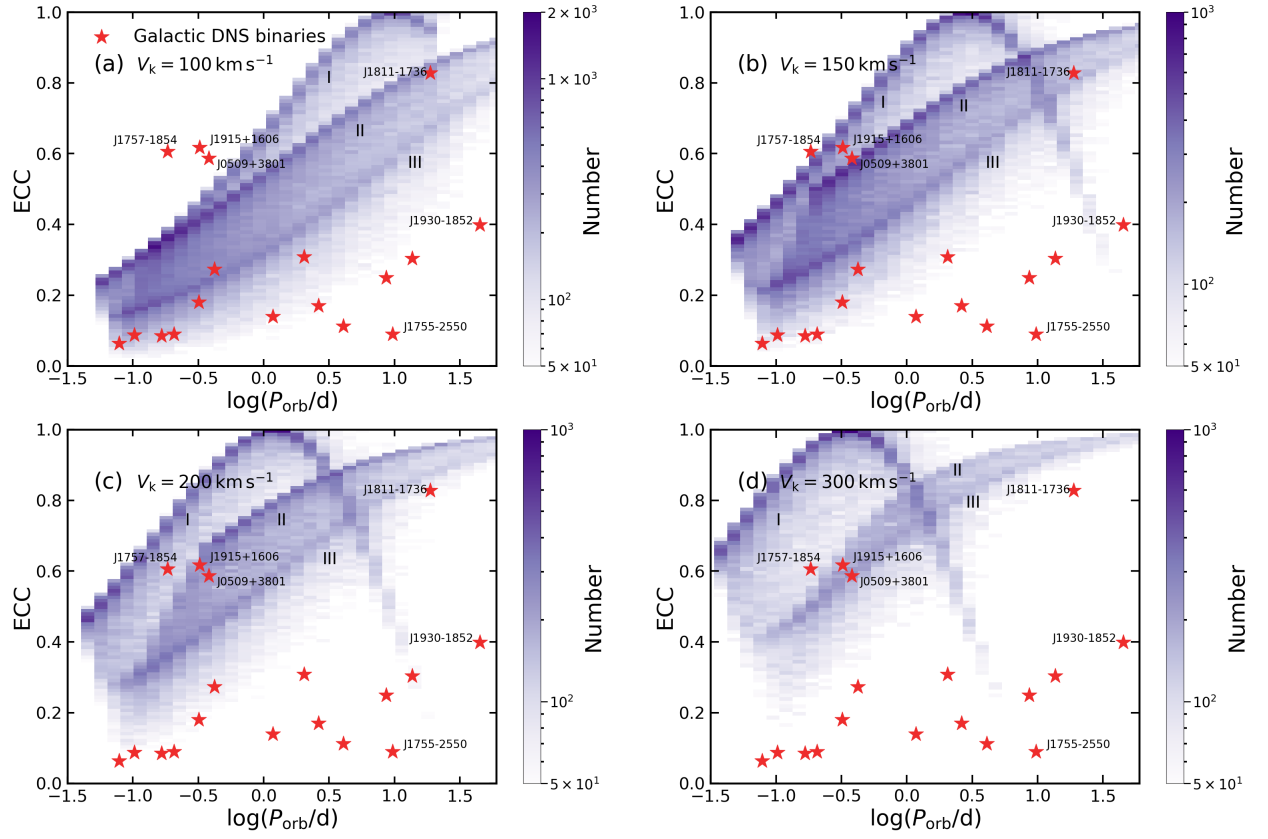


Figure A1. Similar to Fig. 9, but for high NS kick velocities, i.e. $V_k = 100, 200, 300$ and 400 km s^{-1} .

APPENDIX A: THE EFFECT OF HIGHER KICKS AND EJECTED MASS

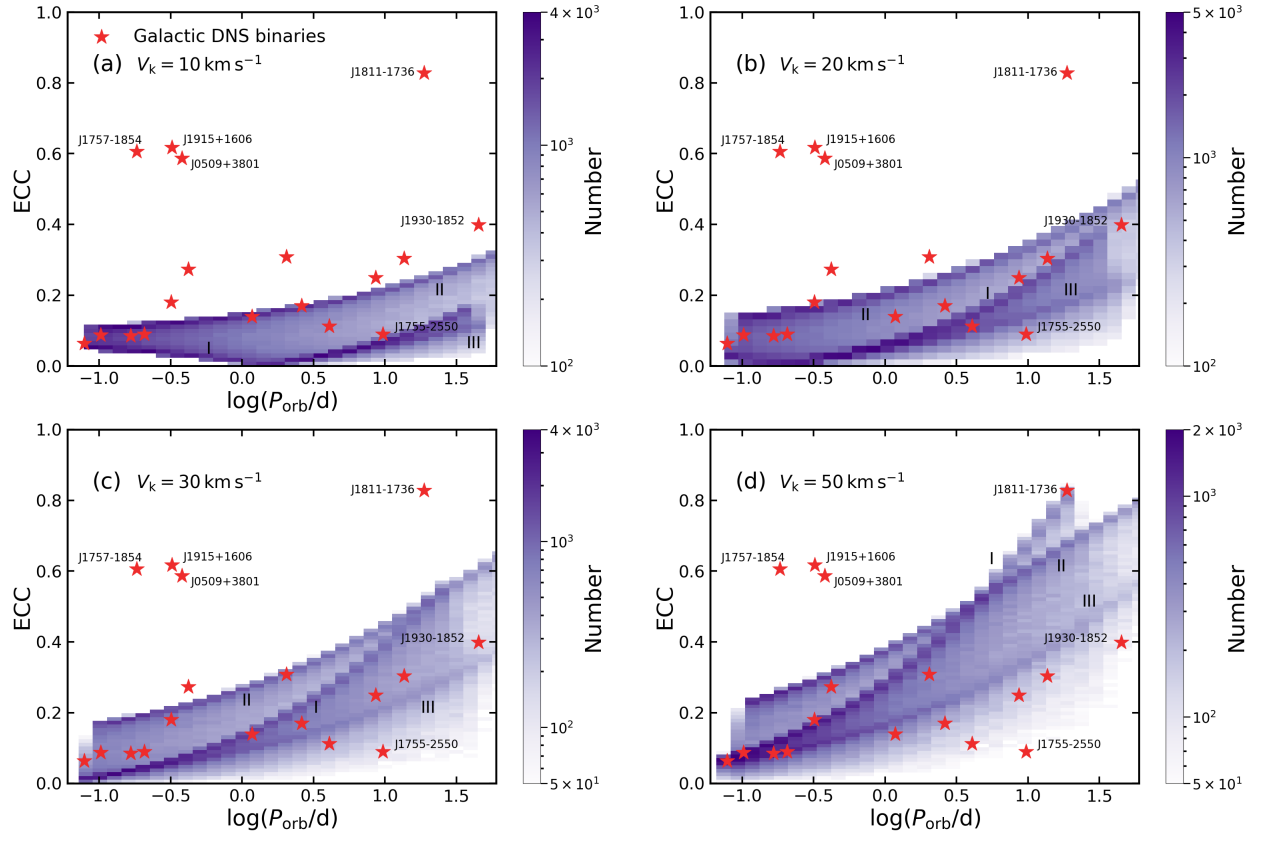


Figure A2. Similar to Fig. 9, but for $\Delta M = 0.2 M_{\odot}$.